

Chiral Phonons in Moiré Superlattices

Nishchay Suri,¹ Chong Wang,² Yinhan Zhang,¹ and Di Xiao^{2,3}

¹*Department of Physics, Carnegie Mellon University, Pittsburgh, Pennsylvania 15213, USA*

²*Department of Materials Science and Engineering,*

University of Washington, Seattle, Washington 98195, USA

³*Department of Physics, University of Washington, Seattle, Washington 98195, USA**

(Dated: December 14, 2021)

We discover chiral phonons at the lowest-energy bands in moiré superlattices. The moiré chiral phonons we uncover are the collective excitations of the stacking domains. Their origin is uniquely attributed to the stacking configurations whose interlayer binding energy breaks the C_{2z} symmetry on the moiré length scale. Within elastic theory, we use a general symmetry analysis to provide a complete classification of van der Waals heterostructures in respect to hosting moiré chiral phonons and show the calculation for twisted MoS₂ as an example. We present a low-energy effective model to qualitatively understand the moiré chiral phonons and show that it captures the essential physics remarkably well. Our result potentially opens up new possibilities in phononic twistrionics as the moiré chiral phonons have high tunability, moiré scale wavelengths, excitation energies in only a few meV, and can possibly be mechanically excited.

When two layers of van der Waals crystals with a small lattice mismatch or rotation are stacked together, a long-wavelength moiré pattern will emerge. The moiré pattern acts like a superlattice potential on charge carriers, which can give rise to a variety of spectacular quantum phenomena [1–3]. The moiré superlattice can also significantly modify the phonon properties, leading to the formation of moiré minibands and strong renormalization of the speed of sound [4–9]. The modification of the low-energy acoustic phonon modes has important implications in thermal transport and electron-phonon interactions in van der Waals heterostructures [10–13].

On the other hand, it has been recently realized that phonons can acquire finite angular momentum and Berry curvature if inversion symmetry is broken [14]. These phonons are called chiral phonons. The angular momentum of chiral phonons decides selection rules in the electronic intervalley scattering [14–19], and their Berry curvature can lead to topological phonon transport [20]. So far, studies of chiral phonons has been focused on crystals with broken sublattice symmetry [14]. The resulting chiral phonon modes are high energy excitations with wavelengths on the order of atomic lattice constant and therefore, they can only be optically excited.

In this Letter, we show that a new type of chiral phonon can emerge in moiré superlattices in van der Waals heterostructures. The moiré chiral phonons we discovered represent the collective motion of the stacking domains. The moiré superlattice causes acoustic branches of the monolayer phonon spectrum to form minibands. We show that these minibands carry chiral phonons that have moiré-scale wavelengths and can possibly be mechanically excited. They originate from stacking configurations whose interlayer binding energy breaks C_{2z} symmetry on the scale of the moiré superlattice. Within the framework of elastic theory, we first present a general symmetry analysis to provide a complete clas-

sification of van der Waals heterostructures according to the existence or absence of chiral moiré phonons. We then demonstrate the existence of these low-energy chiral phonons using twisted bilayer MoS₂ with the twist angle close to 180° as an example. The chiral nature of these phonons is shown by explicit calculation of the phonon angular momentum and Berry curvature, as well as direct visualization of the real-space motion of the phonon modes. To intuitively understand the moiré chiral phonons, we develop a low energy effective model where we show that the interlayer binding potential introduces an antisymmetric term in the effective dynamical matrix which leads to the chirality. Finally, we show the tunability of the moiré chiral phonons by twist angle. The high tunability, excitation energies in only a few meV, superlattice scale wavelengths and possible mechanical excitation of the moiré chiral phonons potentially opens new possibilities in phononic twistrionic devices.

Chiral phonons are characterized by their angular momentum $\mathbf{L}(\mathbf{k})$. For two-dimensional systems, it is sufficient to consider the z component of $\mathbf{L}(\mathbf{k})$. If time-reversal symmetry is present, $L^z(\mathbf{k})$ has the property $L^z(\mathbf{k}) = -L^z(-\mathbf{k})$. If inversion symmetry is also respected, $L^z(\mathbf{k}) = L^z(-\mathbf{k})$, and $L^z(\mathbf{k})$ vanishes. Therefore, it is necessary to break inversion symmetry for the emergence of chiral phonons in non-magnetic systems. The inversion symmetry can be further decomposed into the product of a two-fold rotation C_{2z} around the z axis and a mirror reflection M_z with respect to the xy -plane. It is straightforward to show that C_{2z} also forbids $L^z(\mathbf{k})$ but M_z does not impose any symmetry constraint.

We now apply the above symmetry consideration to moiré phonons. Since we are interested in low-energy phonons on the length scale of the moiré superlattice, we shall adopt the continuum approach based on standard elastic theory [4, 5, 21]. Furthermore, only in-plane

vibrations will be considered because out-of-plane vibrations do not contribute to $L_z(\mathbf{k})$, and the corresponding flexural phonon modes were shown to remain nearly unchanged by the moiré superlattice [4, 9].

The total energy of the system can be separated into an intralayer part and an interlayer part. Introducing the in-plane deformation field $\mathbf{u}^{(\ell)}$ where $\ell \in \{1, 2\}$ is the layer index, the intralayer elastic energy can be expressed as [4, 5, 21]

$$U_E = \sum_{\ell=1}^2 \int d^2r \left[\frac{\lambda^{(\ell)}}{2} (\partial_\alpha u_\alpha^{(\ell)})^2 + \frac{\mu^{(\ell)}}{4} (\partial_\alpha u_\beta^{(\ell)} + \partial_\beta u_\alpha^{(\ell)})^2 \right], \quad (1)$$

where $\mu^{(\ell)}$ and $\lambda^{(\ell)}$ are the Lamé coefficients of layer ℓ . One can see that U_E does not break C_{2z} [22]. It can break M_z if the two layers are different, but the existence of C_{2z} symmetry still forbids the appearance of chiral phonons.

Next we consider the interlayer binding energy. The moiré superlattice can be viewed as a periodic modulation of the local atomic registry, characterized by the relative in-plane displacement $\delta(\mathbf{r})$ between the top and bottom layer. For twisted homobilayers with twist angle θ , $\delta(\mathbf{r}) = [R(\theta) - 1]\mathbf{r} + \mathbf{u}^{(2)}(\mathbf{r}) - \mathbf{u}^{(1)}(\mathbf{r})$, where $R(\theta)$ is the rotation matrix. Within the continuum approximation, the interlayer binding energy can be written as [4, 5, 21]

$$U_B = \int d^2r V[\delta(\mathbf{r})], \quad (2)$$

where $V[\delta]$ is the binding energy density of the rigidly shifted bilayer with shift vector δ . $V[\delta(\mathbf{r})]$ must satisfy the following symmetry constraints. First, moiré patterns created by honeycomb structures has at least three-fold symmetry (Figure 1). Secondly, $V[\delta]$ must remain invariant under a constant displacement of one layer (relative to the other) by an atomic lattice vector. To the lowest order, the Fourier expansion of $V[\delta(\mathbf{r})]$ compatible with three-fold symmetry reads

$$V[\delta(\mathbf{r})] = V_0 \sum_{j=1}^3 \cos[\mathbf{a}_j^* \cdot \delta(\mathbf{r}) + \phi], \quad (3)$$

where \mathbf{a}_j^* are the set of first stars of the reciprocal lattice vectors of the honeycomb structure related by C_{3z} . Crucially, C_{3z} allows a finite phase ϕ , which, except when $\phi = 2n\pi/3$ or $n\pi$ for integer n , breaks C_{2z} symmetry and gives rise to chiral phonons.

Armed with the insight that it is the interlayer binding energy that determines the appearance of chiral phonons, we analyze the symmetry of different types of van der Waals heterostructures. We first consider twisted bilayer graphene. The AA (carbon on carbon) stacking has the highest energy. The local structures at \mathbf{r} and $-\mathbf{r}$ with respect to the location of the AA stacking are exactly the same and are therefore degenerate in stacking energy. This can be seen from Fig. 1(b) by considering the

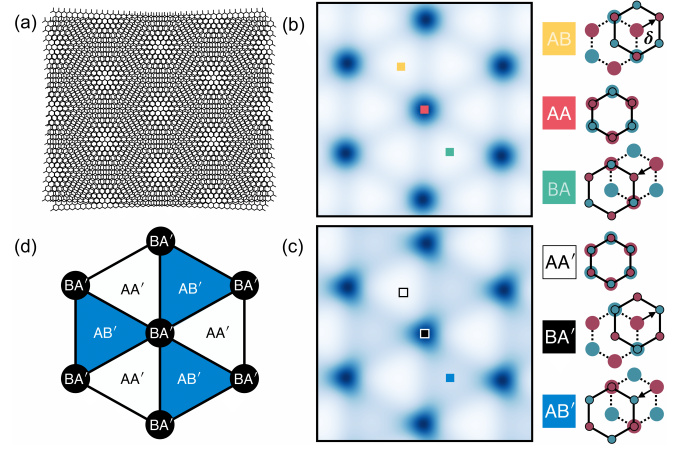


FIG. 1. (a) Moiré pattern of a twisted bilayer h-BN. (b),(c) The interlayer binding potential of the relaxed moiré structure formed by twisting the 0° and 180° configurations, respectively. The colored squares indicate the respective local stackings within the moiré unit cell. The solid lines and smaller circles indicate the top layer, the dashed lines and bigger circles indicate the bottom layer. (d) Schematics of the relaxed moiré superlattice for the 180° configuration.

AB and BA stackings where both sublattices are carbon atoms. In this case, the interlayer binding energy has C_{2z} symmetry and thus, twisted bilayer graphene cannot host moiré chiral phonons. We then consider a twisted homobilayer made of hexagonal-Boron Nitride (h-BN). Since a monolayer h-BN breaks inversion symmetry, the top layer can be initially placed at 0° (AA stacking) or 180° (AA' stacking) with respect to the bottom layer and then twisted to form two different moiré superlattices. For the 0° orientation, even though the local structures at \mathbf{r} and $-\mathbf{r}$ are no longer identical, they are M_z images of each other, therefore the stacking potential still respects C_{2z} symmetry. This can be seen, for example, by considering again the AB and BA stacking, as marked by yellow and green squares in Figure 1(b). Under M_z , the AB and BA stacking transform into each other, therefore they must have the same stacking energy. For the 180° configuration the local structures at \mathbf{r} and $-\mathbf{r}$ are not related by M_z anymore. Figure 1(c) shows that the AB' and BA' stackings are not M_z images. In fact, the AA' stacking is the energy minimum and BA' is the energy maximum [23]. In this case, the interlayer binding energy breaks C_{2z} symmetry, permitting the appearance of chiral phonons. The same symmetry analysis also applies to twisted transition metal dichalcogenides (TMDs)[24].

Finally, we consider heterobilayers such as graphene/h-BN or any combination of TMDs. In this case, the AB' and BA' stackings are no longer related by M_z , and C_{2z} is broken irrespective of the initial orientation. Therefore, chiral phonons must be a possibility. In addition, the breaking of M_z symmetry can lead to interesting layer-dependent phenomena that will be explored elsewhere.

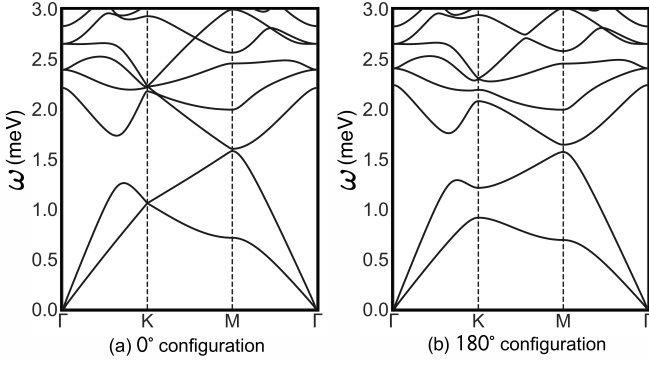


FIG. 2. The moiré phonon band structures at twist angle $\theta = 2^\circ$ for (a) the 0° configuration and (b) the 180° configuration. The lowest two bands are degenerate at the \mathbf{K} point in (a) while in (b) this degeneracy is lifted.

As a specific example, we calculate the phonon spectrum for a twisted homobilayer. The Lagrangian is written as

$$\mathcal{L} = K - U_E - U_B, \quad (4)$$

where $K = (1/2) \int d^2r \sum_\ell \rho^{(\ell)} (\dot{\mathbf{u}}^{(\ell)})^2$ is the kinetic energy of the system. It is convenient to change the basis to symmetric and antisymmetric modes defined as $\mathbf{u}^\pm = \mathbf{u}^{(1)} \pm \mathbf{u}^{(2)}$. For twisted homobilayers, the moiré potential will only affect the \mathbf{u}^- mode. We express $\mathbf{u}^-(\mathbf{r}, t) = \mathbf{u}_0^-(\mathbf{r}) + \delta\mathbf{u}^-(\mathbf{r}, t)$, where \mathbf{u}_0^- is the static part describing lattice relaxation and $\delta\mathbf{u}^-$ is the dynamical part describing phonons. The calculation follows the procedure outlined in Ref. [4] and the details can be found in the Supplementary Material [25].

We show the calculation of twisted MoS₂ for both the 0° and 180° configurations with a 2° twist angle. For MoS₂, the density $\rho = 3.026 \times 10^{-6}$ kg/m² and Lamé coefficients are $\lambda = 3.3$ eV/Å² and $\mu = 3.6$ eV/Å². The binding energy of the 180° configuration are specified by $V_0 = 1.4$ meV and $\phi = -11.04^\circ$ [21]. For the 0° configuration we use the same V_0 but set $\phi = 0$. We first relax the lattice structure, which leads to the formation of large stacking domains. The resulting interlayer binding potentials are shown in Figure 1(b) and (c) for the 0° and the 180° configuration, respectively. It can be seen that the 0° configuration preserves C_{2z} while the 180° configuration breaks it. This symmetry difference is reflected in the phonon band structures as shown in Figure 2. The two lowest bands are degenerate at the \mathbf{K} point for the 0° configuration but split up for the 180° configuration due to the breaking of C_{2z} , signifying the appearance of chiral phonons.

To verify that phonons of the 180° configuration are indeed chiral, we calculate their angular momentum, de-

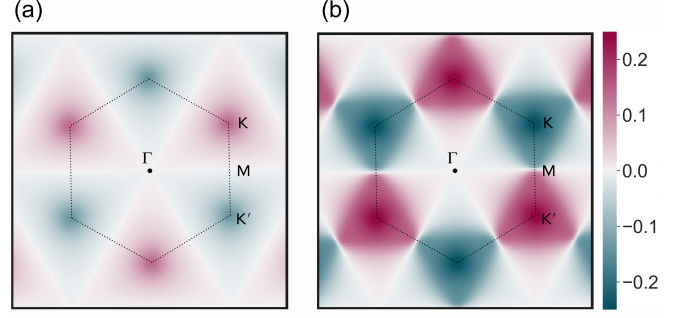


FIG. 3. The angular momentum (\hbar) of (a) the lowest and (b) the second lowest phonon band in the reciprocal space for the 180° twisted bilayer MoS₂ at twist angle $\theta = 2^\circ$.

fined at momentum \mathbf{q} as [25, 26]

$$L_{\sigma\mathbf{q}}^z = \rho \int d^2r \sum_{\ell=1}^2 (\delta\mathbf{u}_{\sigma\mathbf{q}}^{(\ell)} \times \delta\dot{\mathbf{u}}_{\sigma\mathbf{q}}^{(\ell)})_z, \quad (5)$$

where $u_{\sigma\mathbf{q}}$ is the eigenmode of the σ th branch. Figure 3 shows the angular momentum of the two lowest bands in the reciprocal space. We see that the angular momentum has opposite sign at opposite momentum, as dictated by time-reversal symmetry. The angular momentum of the lowest band is more localized around the corners of the Brillouin zone compared to the second lowest band, due to the latter's proximity to the third band in energy. We have also calculated the phonon Berry curvature [25], which shows the same symmetry property as $L_{\mathbf{q}}^z$ and can lead to a phonon angular momentum Hall effect.

To gain further insight into the formation of chiral phonons, we plot $\delta\mathbf{u}^-(\mathbf{r}, t)$ of the lowest phonon mode at the \mathbf{K} point in Figure 4(a) and (b). We see that the BA' regions rotate anticlockwise while the AA' regions rotate clockwise with a much smaller amplitude, and the AB' regions remain stationary. As a result, the phonon mode carries a net angular momentum. For the next band, we find opposite behavior: the BA' regions rotate clockwise; the AA' regions remain stationary and the AB' regions rotate anticlockwise with a much smaller amplitude. A movie showing their full motion in time can be found in the Supplementary Material [25].

Based on the real-space picture, we develop a low-energy effective model to provide an intuitive explanation for the emergence of chiral phonons. Since the angular momentum is mainly carried by the motion of the BA' regions, the chiral phonon mode can be qualitatively understood by taking the BA' regions as oscillating 'points' with displacements $\tilde{\mathbf{u}}(\mathbf{R})$. The BA' oscillators are connected by domain walls that separate the AA' and AB' domains as shown in Figure 4(c). The potential energy of the system comes from two parts: the domain walls and the domains. The domain wall energy has been considered previously by Koshino and Son [4]; it is written

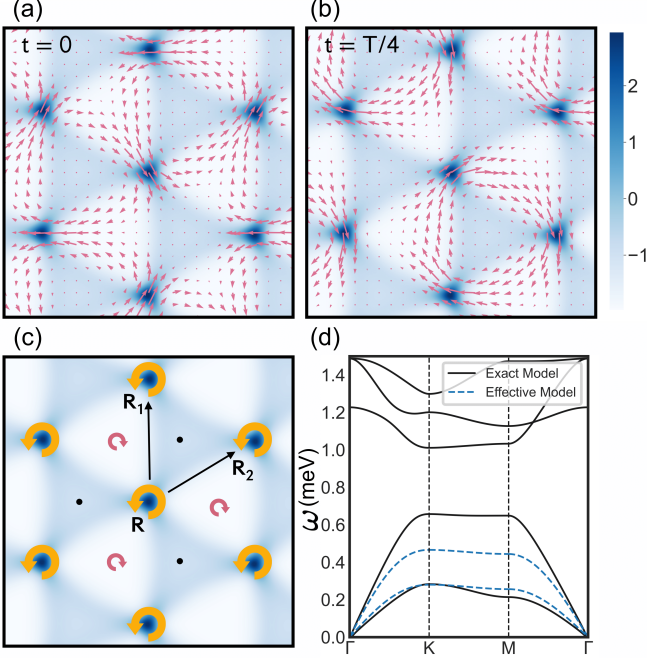


FIG. 4. The real space displacement field $\delta \mathbf{u}^-(\mathbf{r}, t)$ of the lowest band at the \mathbf{K} point at times (a) $t = 0$ and (b) $t = T/4$ respectively, where T is the time period. The twist angle is 1° for the 180° configuration. The background is the interlayer binding potential of the relaxed structure. The dark blue regions are BA', the bigger white regions are AA' and the smaller light blue regions are AB'. (c) Schematics of phonon modes show the rotation of different stacking regions. The size of arrows represents the amplitude and the black dots represent the lack of motion. (d) The band structure for the low energy effective model compared with the exact calculation.

as $E_{\text{DW}} = (1/2) \sum_{\mathbf{q}} \tilde{\mathbf{u}}_{-\mathbf{q}}^T D^{\text{DW}}(\mathbf{q}) \tilde{\mathbf{u}}_{\mathbf{q}}$, where the dynamical matrix $D^{\text{DW}}(\mathbf{q})$ was derived in Ref. 4 and reproduced in the Supplementary Material [25]. It satisfies the property $D^{\text{DW}}(\mathbf{q}) = D^{\text{DW}}(-\mathbf{q})$, i.e., E_{DW} does not break C_{2z} . The key to understand the emergence of chirality lies in the potential energy associated with the domains. During the oscillation of the domain wall network, the areas of stacking domains AA' and AB' will change. This leads to an additional change of the potential energy given by $E_{\text{Domain}} = V_{AA'} \Delta A_{AA'} + V_{AB'} \Delta A_{AB'}$, where V and ΔA are the average potential and change in area of the respective domains. Let us consider a triangle defined by the three points \mathbf{R} , \mathbf{R}_1 and \mathbf{R}_2 shown in Figure 4(c). Simple geometric consideration yields the change in area as $\Delta A = (1/2)[(\tilde{\mathbf{u}}(\mathbf{R}_1) - \tilde{\mathbf{u}}(\mathbf{R})) \times (\tilde{\mathbf{u}}(\mathbf{R}_2) - \tilde{\mathbf{u}}(\mathbf{R}))] \cdot \mathbf{z}$, in which we only kept bilinear terms in displacement field as the linear terms average out to zero. Transforming to Fourier space, the potential energy associated with do-

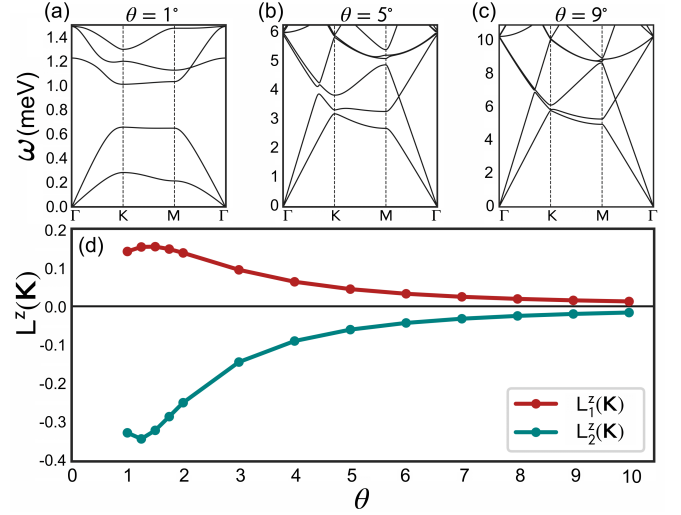


FIG. 5. (a)-(c) The moiré phonon band structures at various twist angles for twisted bilayer MoS₂ in the 180° configuration. (d) The angular momentum (\hbar) of the lowest two bands at the \mathbf{K} point as a function of twist angle.

main reads [25]

$$E_{\text{Domain}} = \alpha \frac{(V_{AA'} - V_{AB'})}{2} \sum_{\mathbf{q}} \tilde{\mathbf{u}}_{-\mathbf{q}}^T \begin{bmatrix} 0 & \gamma(\mathbf{q}) \\ -\gamma(\mathbf{q}) & 0 \end{bmatrix} \tilde{\mathbf{u}}_{\mathbf{q}}, \quad (6)$$

where $\gamma(\mathbf{q}) = 4i \sin[\mathbf{q} \cdot (\mathbf{L}_2 - \mathbf{L}_1)/2] \sin(\mathbf{q} \cdot \mathbf{L}_1/2) \sin(\mathbf{q} \cdot \mathbf{L}_2/2)$, α is an overall fitting parameter to match the energy, and \mathbf{L}_1 and \mathbf{L}_2 are moiré lattice vectors. This term is proportional to the stacking energy difference between the AA' and AB' domains and, therefore, owes its origin to the asymmetric interlayer binding potential. It breaks C_{2z} , which opens the band gap at the \mathbf{K} point and gives rise to chiral phonons. We solve the effective model [25] and plot the phonon band dispersion together with that from the elastic theory calculation in Figure 4(d). The agreement is remarkably well given the simplicity of the effective model.

Finally, we show in Figure 5 the tunability of chiral phonons with respect to the twist angle θ . As θ decreases, the BA' regions responsible for larger part of the angular momentum decrease in area. The AA' and AB' regions responsible for smaller counter angular momentum in the first two bands respectively increase in area. Moreover, the area of AA' regions increase more than the AB' regions due to the former's lower stacking energy. This leads to a non-monotonic and asymmetric dependence of angular momentum of the lowest two bands on twist angle. In addition, the second-lowest band is not entirely separate from the bands above it and therefore its angular momentum does not cancel the angular momentum of the lowest band exactly.

In summary, we showed that chiral phonons can emerge at the moiré wavelength in van der Waals het-

erostuctures due to C_{2z} symmetry breaking of the interlayer binding energy. We used elastic theory to calculate the phonon spectrum for twisted bilayer MoS_2 and verified the chiral nature of these phonons by calculating their angular momentum. The formation of the chiral phonons can be qualitatively understood using an effective model, which emphasizes their origin in the energy difference between the two stacking domains. Compared to the original proposal of chiral phonons in monolayer TMDs [14], the moiré chiral phonons have high tunability, excitation energies in only a few meV, superlattice scale wavelengths and can possibly be mechanically excited. They potentially open new possibilities in phononic twistrionic devices.

We are grateful to Hector Ochoa and Haidan Wen for fruitful discussions. This work was supported by the Department of Energy, Basic Energy Sciences, Materials Sciences and Engineering Division, Pro-QM EFRC (DE-SC0019443). C.W. acknowledges the support from the Department of Energy, Basic Energy Sciences, Materials Sciences and Engineering Division (DE-SC0012509).

Note added.—Upon the completion of our work, we become aware of a recent preprint in which chiral phonons in moiré superlattices was discussed using interatomic force-field based simulations [27].

* dixiao@uw.edu

- [1] E. Y. Andrei and A. H. MacDonald, Graphene bilayers with a twist, *Nat. Mater.* **19**, 1265 (2020).
- [2] L. Balents, C. R. Dean, D. K. Efetov, and A. F. Young, Superconductivity and strong correlations in moiré flat bands, *Nat. Phys.* **16**, 725 (2020).
- [3] D. M. Kennes, M. Claassen, L. Xian, A. Georges, A. J. Millis, J. Hone, C. R. Dean, D. Basov, A. N. Pasupathy, and A. Rubio, Moiré heterostructures as a condensed-matter quantum simulator, *Nat. Phys.* **17**, 155 (2021).
- [4] M. Koshino and Y.-W. Son, Moiré phonons in twisted bilayer graphene, *Phys. Rev. B* **100**, 075416 (2019).
- [5] H. Ochoa, Moiré-pattern fluctuations and electron-phonon coupling in twisted bilayer graphene, *Phys. Rev. B* **100**, 155426 (2019).
- [6] I. Maity, M. H. Naik, P. K. Maiti, H. Krishnamurthy, and M. Jain, Phonons in twisted transition-metal dichalcogenide bilayers: Ultrasoft phasons and a transition from a superlubric to a pinned phase, *Phys. Rev. Research* **2**, 013335 (2020).
- [7] M. Lamparski, B. Van Troeye, and V. Meunier, Soliton signature in the phonon spectrum of twisted bilayer graphene, *2D Mater.* **7**, 025050 (2020).
- [8] A. C. Gadelha, D. A. Ohlberg, C. Rabelo, E. G. Neto, T. L. Vasconcelos, J. L. Campos, J. S. Lemos, V. Ornelas, D. Miranda, R. Nadas, *et al.*, Localization of lattice dynamics in low-angle twisted bilayer graphene, *Nature* **590**, 405 (2021).
- [9] J. Quan, L. Linhart, M.-L. Lin, D. Lee, J. Zhu, C.-Y. Wang, W.-T. Hsu, J. Choi, J. Embley, C. Young, *et al.*, Phonon renormalization in reconstructed mos_2 moiré superlattices, *Nat. Mater.* **20**, 1100 (2021).
- [10] F. Wu, A. H. MacDonald, and I. Martin, Theory of phonon-mediated superconductivity in twisted bilayer graphene, *Phys. Rev. Lett.* , 257001 (2018).
- [11] B. Lian, Z. Wang, and B. A. Bernevig, Twisted bilayer graphene: A phonon-driven superconductor, *Phys. Rev. Lett.* **122**, 257002 (2019).
- [12] F. Wu, E. Hwang, and S. Das Sarma, Phonon-induced giant linear-in- t resistivity in magic angle twisted bilayer graphene: Ordinary strangeness and exotic superconductivity, *Phys. Rev. B* **99**, 165112 (2019).
- [13] M. Koshino and N. N. T. Nam, Effective continuum model for relaxed twisted bilayer graphene and moiré electron-phonon interaction, *Phys. Rev. B* **101**, 195425 (2020).
- [14] L. Zhang and Q. Niu, Chiral phonons at high-symmetry points in monolayer hexagonal lattices, *Phys. Rev. Lett.* **115**, 115502 (2015).
- [15] H. Zhu, J. Yi, M.-Y. Li, J. Xiao, L. Zhang, C.-W. Yang, R. A. Kaindl, L.-J. Li, Y. Wang, and X. Zhang, Observation of chiral phonons, *Science* **359**, 579 (2018).
- [16] X. Chen, X. Lu, S. Dubey, Q. Yao, S. Liu, X. Wang, Q. Xiong, L. Zhang, and A. Srivastava, Entanglement of single-photons and chiral phonons in atomically thin WSe_2 , *Nat. Phys.* **15**, 221 (2019).
- [17] M. He, P. Rivera, D. Van Tuan, N. P. Wilson, M. Yang, T. Taniguchi, K. Watanabe, J. Yan, D. G. Mandrus, H. Yu, *et al.*, Valley phonons and exciton complexes in a monolayer semiconductor, *Nat. Commun.* **11**, 618 (2020).
- [18] E. Liu, J. van Baren, C.-T. Liang, T. Taniguchi, K. Watanabe, N. M. Gabor, Y.-C. Chang, and C. H. Lui, Multipath optical recombination of intervalley dark excitons and trions in monolayer wse_2 , *Phys. Rev. Lett.* **124**, 196802 (2020).
- [19] A. Delhomme, D. Vaclavkova, A. Slobodeniuk, M. Orlita, M. Potemski, D. Basko, K. Watanabe, T. Taniguchi, D. Mauro, C. Barreteau, *et al.*, Flipping exciton angular momentum with chiral phonons in $\text{MoSe}_2/\text{WSe}_2$ heterobilayers, *2D Mater.* **7**, 041002 (2020).
- [20] X. Li, C. Xia, Y. Pan, M. Gao, H. Chen, and L. Zhang, Topological chiral phonons along the line defect of intralayer heterojunctions, *Phys. Rev. B* **104**, 054103 (2021).
- [21] S. Carr, D. Massatt, S. B. Torrisi, P. Cazeaux, M. Luskin, and E. Kaxiras, Relaxation and domain formation in incommensurate two-dimensional heterostructures, *Phys. Rev. B* **98**, 224102 (2018).
- [22] Materials like monolayer hexagonal boron nitride(h-BN) indeed break inversion symmetry on atomic scale. However, the theory of elasticity is a macroscopic continuum theory concerned with distances much larger than the atomic scale. It provides a useful and correct description of the low energy and long-wavelength acoustic vibrations where the variation in deformation is smooth and small as compared to the distances. It is therefore oblivious to inversion breaking on the atomic scale.
- [23] G. Constantinescu, A. Kuc, and T. Heine, Stacking in bulk and bilayer hexagonal boron nitride, *Phys. Rev. Lett.* **111**, 036104 (2013).
- [24] V. V. Enaldiev, V. Zólyomi, C. Yelgel, S. J. Magorrian, and V. I. Fal'ko, Stacking domains and dislocation networks in marginally twisted bilayers of transition metal dichalcogenides, *Phys. Rev. Lett.* **124**, 206101 (2020).
- [25] Supplimentary Materials.

- [26] L. Zhang and Q. Niu, Angular momentum of phonons and the einstein–de haas effect, *Phys. Rev. Lett.* **112**, 085503 (2014).
- [27] I. Maity, A. A. Mostofi, and J. Lischner, Chiral valley phonons and flat phonon bands in moire materials, 2021, arXiv: 2108.03965. arXiv.org e-Print archive. <https://arxiv.org/abs/2108.03965> (accessed Nov 8, 2021)., arXiv:2108.03965 [cond-mat.mtrl-sci].

Supporting Information: Chiral Phonons in Moiré Superlattices

Nishchay Suri,¹ Chong Wang,² Yinhan Zhang,¹ and Di Xiao^{2,3}

¹*Department of Physics, Carnegie Mellon University, Pittsburgh, Pennsylvania 15213, USA*

²*Department of Materials Science and Engineering,*

University of Washington, Seattle, Washington 98195, USA

³*Department of Physics, University of Washington, Seattle, Washington 98195, USA**

(Dated: December 14, 2021)

PHONONS IN MOIRÉ SUPERLATTICES

In this section we present a detailed derivation of the moiré phonon band structures, following Ref. 1 and 2. Let us consider the case of twisted homobilayers. We define the primitive lattice vectors of layer 1 as

$$\mathbf{a}_1 = a(1, 0), \quad \mathbf{a}_2 = a(1/2, \sqrt{3}/2). \quad (\text{S1})$$

The reciprocal lattice vectors of layer 1 are given as

$$\mathbf{a}_1^* = 2\pi/a(1, -1/\sqrt{3}), \quad \mathbf{a}_2^* = 2\pi/a(0, 2/\sqrt{3}). \quad (\text{S2})$$

As a result of the twist, an atom on layer 2 originally located at \mathbf{r}_0 is moved to $\mathbf{r} = R(\theta)\mathbf{r}_0$, where $R(\theta)$ is the rotation matrix. Then, we define the interlayer atomic shift given by $\delta(\mathbf{r})$ as the in-plane position of an atom on layer 2 measured from its counterpart in layer 1. In the case of pure rotation we have

$$\delta_0(\mathbf{r}) = \mathbf{r} - \mathbf{r}_0 = (1 - R^{-1}(\theta))\mathbf{r}. \quad (\text{S3})$$

The moiré lattice and reciprocal lattice vectors are given as

$$\mathbf{L}_i = (1 - R^{-1}(\theta))^{-1}\mathbf{a}_i, \quad \mathbf{G}_i = (1 - R(\theta))\mathbf{a}_i^*, \quad (\text{S4})$$

respectively.

The total instantaneous interlayer atomic shift is given by $\delta(\mathbf{r}) = \delta_0(\mathbf{r}) + \mathbf{u}^-(\mathbf{r}, t)$, where $\mathbf{u}^- = \mathbf{u}^{(2)} - \mathbf{u}^{(1)}$ is the relative deformation field. The Lagrangian density is composed of the kinetic energy K , intra-layer elastic energy U_E and the inter-layer binding energy U_B ,

$$\mathcal{L} = K - U_E - U_B, \quad (\text{S5})$$

$$K = \int d^2r \frac{\rho}{2} \sum_{\ell=1}^2 (\dot{\mathbf{u}}^{(\ell)})^2, \quad (\text{S6})$$

$$U_E = \int d^2r \sum_{\ell=1}^2 \left\{ \frac{\lambda}{2} \left(\partial_\alpha u_\alpha^{(\ell)} \right)^2 + \frac{\mu}{4} \left(\partial_\alpha u_\beta^{(\ell)} + \partial_\beta u_\alpha^{(\ell)} \right)^2 \right\}, \quad (\text{S7})$$

$$U_B = \int d^2r V_0 \sum_{j=1}^3 \cos(\mathbf{a}_j^* \cdot \delta(\mathbf{r}) + \phi), \quad (\text{S8})$$

where ℓ is the layer index, ρ is the density, and μ, λ are the Lamé coefficients. Similar to \mathbf{u}^- , it is convenient to define $\mathbf{u}^+ = \mathbf{u}^{(2)} + \mathbf{u}^{(1)}$ and write the above energies and equations in these coordinates:

$$K = \int d^2r \frac{\rho}{4} \sum_{l=1}^2 (\dot{\mathbf{u}}^{+2} + \dot{\mathbf{u}}^{-2}), \quad (\text{S9})$$

$$U_E = \int d^2r \frac{1}{2} \left\{ \frac{\lambda}{2} [(\partial_\alpha u_\alpha^+)^2 + (\partial_\alpha u_\alpha^-)^2] + \frac{\mu}{4} [(\partial_\alpha u_\beta^+ + \partial_\beta u_\alpha^+)^2 + (\partial_\alpha u_\beta^- + \partial_\beta u_\alpha^-)^2] \right\}, \quad (\text{S10})$$

$$U_B = \int d^2r V_0 \sum_{j=1}^3 \cos(\mathbf{G}_j \cdot \mathbf{r} + \mathbf{a}_j^* \cdot \mathbf{u}^- + \phi). \quad (\text{S11})$$

* dixiao@uw.edu

Since mirror z symmetry is present in elastic theory, \mathbf{u}^+ and \mathbf{u}^- modes are completely decoupled. The \mathbf{u}^+ mode is unaffected by the binding energy; it can be ignored as its phonon dispersion will be the zone folded monolayer dispersion. In the following we will only focus on the \mathbf{u}^- mode.

We express $\mathbf{u}^-(\mathbf{r}, t) = \mathbf{u}_0^-(\mathbf{r}) + \delta\mathbf{u}^-(\mathbf{r}, t)$, where \mathbf{u}_0^- is the equilibrium part describing the lattice relaxation and $\delta\mathbf{u}^-$ is the dynamical part describing phonons. Using the Euler-Lagrange equations for \mathbf{u}_0^- , we obtain:

$$\mu\partial_\beta^2 u_{0\alpha}^- + (\mu + \lambda)\partial_\alpha\partial_\beta u_{0\beta}^- + 2V_0 \sum_j (a_j^*)_\alpha \sin(\mathbf{G}_j \cdot \mathbf{r} + \mathbf{a}_j^* \cdot \mathbf{u}_0^- + \phi) = 0. \quad (\text{S12})$$

To solve for the relaxed structure we transform to Fourier space and proceed to solve a system of self-consistent equations. We write $\mathbf{u}_0^- = \sum_{\mathbf{G}} \mathbf{u}_{0\mathbf{G}}^- e^{i\mathbf{G} \cdot \mathbf{r}}$ where $\mathbf{G} = m\mathbf{G}_1 + n\mathbf{G}_2$, such that $m, n \in \mathbb{Z}$. We note that with enough harmonics we can get the relaxation to converge, leading to an all real phonon spectrum which is physical. For the calculation shown in main text, it suffices to take $m, n \in \{\pm 1, \dots, \pm 20\}$ for the most strongly relaxed 1° twist configuration. Since ϕ breaks the six-fold symmetry, we impose C_3 constraint on \mathbf{u}_0^- :

$$R_{\frac{2\pi}{3}} \mathbf{u}_{0,\mathbf{q}}^- = \mathbf{u}_{0,R_{\frac{2\pi}{3}}\mathbf{q}}^-, \quad (\text{S13})$$

where $R_{\frac{2\pi}{3}}$ is the rotation matrix. It can further be shown that the equation for phonon dynamics is

$$\rho\delta\ddot{u}_\alpha^- = \mu\partial_\beta^2 \delta u_\alpha^- + (\mu + \lambda)\partial_\alpha\partial_\beta \delta u_\beta^- + 2V_0 \sum_j (a_j^*)_\alpha (a_j^*)_\beta \cos(\mathbf{G}_j \cdot \mathbf{r} + \mathbf{a}_j^* \cdot \mathbf{u}_0^- + \phi) \delta u_\beta^-. \quad (\text{S14})$$

We expand the above equation in Fourier series,

$$\delta\mathbf{u}^-(\mathbf{r}, t) = e^{-i\omega t} \sum_{\mathbf{q}} \boldsymbol{\epsilon}^-(\mathbf{q}) e^{i\mathbf{q} \cdot \mathbf{r}}, \quad (\text{S15})$$

$$\cos(\mathbf{G}_j \cdot \mathbf{r} + \mathbf{a}_j^* \cdot \mathbf{u}_0^- + \phi) = \sum_{\mathbf{G}} h_{\mathbf{G}}^j e^{i\mathbf{G} \cdot \mathbf{r}}, \quad (\text{S16})$$

$$\rho\omega^2 \epsilon_\alpha^-(\mathbf{q}) = \mu q_\beta^2 \epsilon_\alpha^-(\mathbf{q}) + (\mu + \lambda) q_\alpha q_\beta \epsilon_\beta^-(\mathbf{q}) - 2V_0 \sum_{j\mathbf{G}} (a_j^*)_\alpha (a_j^*)_\beta h_{\mathbf{G}}^j \epsilon_\beta^-(\mathbf{q} - \mathbf{G}), \quad (\text{S17})$$

where $\mathbf{G} = m\mathbf{G}_1 + n\mathbf{G}_2$ and $m, n \in \mathbb{Z}$. The solution of the above central equation is given by the set of eigenfunctions

$$\delta\mathbf{u}_{\sigma\mathbf{q}}^-(\mathbf{r}) = e^{-i\omega t} \sum_{\mathbf{G}} \boldsymbol{\epsilon}_{\sigma,\mathbf{q}-\mathbf{G}}^- e^{i(\mathbf{q}-\mathbf{G}) \cdot \mathbf{r}}, \quad (\text{S18})$$

for eigenvalues $\omega_\sigma^2(\mathbf{q})$ where σ is the band index.

For the actual calculations we considered twisted bilayer MoS₂. For MoS₂, $a = 3.18\text{\AA}$. The density $\rho = 3.026 \times 10^{-6} \text{ kg/m}^2$. The Lamé constants are given by $\lambda = 3.3 \text{ eV/\AA}^2$, $\mu = 3.6 \text{ eV/\AA}^2$. The parameters for binding energy are given by Ref. 3:

$$\Delta = \sum_{i=1}^3 [\Delta_1 \cos(\mathbf{G}_i \cdot \mathbf{r} + \mathbf{a}_i^* \cdot \mathbf{u}^-) + \Delta_2 \sin(\mathbf{G}_i \cdot \mathbf{r} + \mathbf{a}_i^* \cdot \mathbf{u}^-)] / \text{Area} \quad (\text{S19})$$

$$= V_0 \sum_{i=1}^3 \cos(\mathbf{G}_i \cdot \mathbf{r} + \mathbf{a}_i^* \cdot \mathbf{u}^- + \phi) \quad (\text{S20})$$

$$= V_0 \sum_{i=1}^3 (\cos(\mathbf{G}_i \cdot \mathbf{r} + \mathbf{a}_i^* \cdot \mathbf{u}^-) \cos(\phi) - \sin(\mathbf{G}_i \cdot \mathbf{r} + \mathbf{a}_i^* \cdot \mathbf{u}^-) \sin(\phi)). \quad (\text{S21})$$

Using the relations $V_0 = \sqrt{\Delta_1^2 + \Delta_2^2} / \text{unit cell area}$ and $\tan \phi = -\Delta_2 / \Delta_1$. For 0° MoS₂, with $\Delta_1 = 0.014 \text{ eV}$, $\Delta_2 = 0$, we obtain $V_0 = 1.6 \text{ meV/\AA}^2$ and $\phi = 0^\circ$. For 180° MoS₂, with $\Delta_1 = 0.0123 \text{ eV}$, $\Delta_2 = 0.0024 \text{ eV}$, we obtain $V_0 = 1.4 \text{ meV/\AA}^2$ and $\phi = -11.04^\circ$. In our calculation of the phonon spectrum (Fig. 2 in main text), we used the same $V_0 = 1.4 \text{ meV/\AA}^2$ for both configurations to illustrate the effect of inversion symmetry breaking (finite ϕ). The real space phonon field for the second and third lowest bands are shown in Fig. S1. To demonstrate the chirality of respective domains, the fields for each band are plotted for times $t = 0$ and $t = T/4$, where T is the time period.

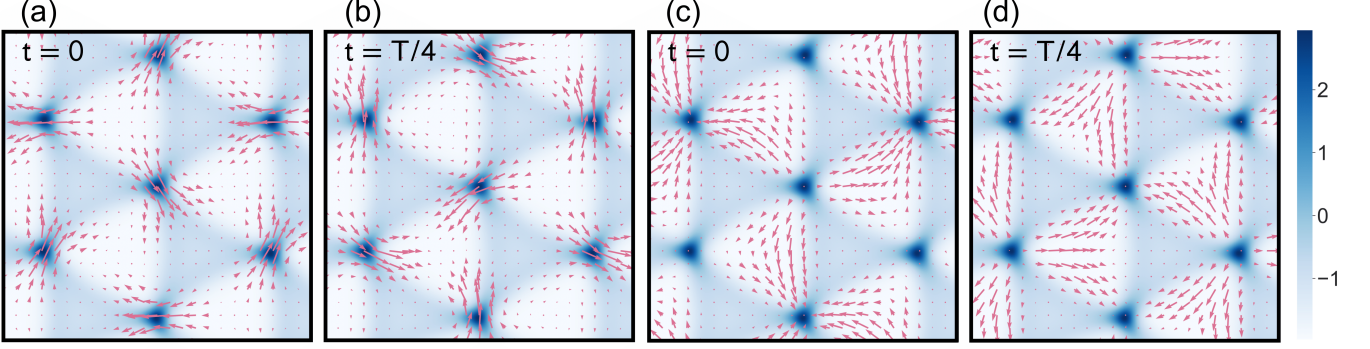


FIG. S1. The twist angle is 1° for the 180° configuration MoS_2 . The background is the interlayer binding potential of the relaxed structure. The dark blue regions are BA' , the bigger white regions are AA' and the smaller light blue regions are AB' . The real space displacement field $\delta \mathbf{u}^-(\mathbf{r}, t)$ of the second lowest band at the \mathbf{K} point at times (a) $t = 0$ and (b) $t = T/4$ respectively, where T is the time period. The real space displacement field for the third lowest band at times (c) $t = 0$ and (d) $t = T/4$ respectively.

ANGULAR MOMENTUM

In this section we present the detailed steps on the calculation of phonon angular momentum shown in Fig. 3 and Fig. 5 in the main text. The phonon angular momentum is defined as [4, 5]:

$$L^z = \rho \int d^2 \mathbf{r} \sum_{\ell=1,2} (\delta u_x^{(\ell)} \delta \dot{u}_y^{(\ell)} - \delta u_y^{(\ell)} \delta \dot{u}_x^{(\ell)}) = \rho \int d^2 \mathbf{r} \delta u^T(\mathbf{r}) i M \delta \dot{\mathbf{u}}(\mathbf{r}), \quad (\text{S22})$$

where $M = I_2 \otimes \sigma_y$ and $\delta u(\mathbf{r}) = [\delta u_x^{(1)}(\mathbf{r}), \delta u_y^{(1)}(\mathbf{r}), \delta u_x^{(2)}(\mathbf{r}), \delta u_y^{(2)}(\mathbf{r})]^T$. For the unit cell number n and the sublattice atom number α , we have

$$\delta u_{n,\alpha} = \sum_k \tilde{\epsilon}_{k,\alpha} e^{i(\mathbf{k} \cdot \mathbf{R}_n - \omega_k t)} \sqrt{\frac{\hbar}{2\omega_k m_\alpha N}} a_k + h.c., \quad (\text{S23})$$

where $k = (\mathbf{k}, \sigma)$, σ is the band number, m_α is the mass of the α^{th} atom and N is the number of unit cells. The eigenfunction $\tilde{\epsilon}_{k\alpha} = \sum_{\mathbf{G}} \epsilon_{k\mathbf{G}} e^{i(\mathbf{k} - \mathbf{G}) \cdot \mathbf{r}_\alpha}$, where $\epsilon_{k\mathbf{G}}$ are the coefficients of the block function solution to the central equation. The $\epsilon_{k\mathbf{G}}$ can be obtained from Eq. S18 by setting $\mathbf{u}^+ = 0$ as we are calculating angular momentum for the \mathbf{u}^- bands. The $\epsilon_{k\mathbf{G}}$ are normalized with respect to harmonics \mathbf{G} . The vector \mathbf{r}_α points to the α^{th} atom in moiré unit cell. In the case where all sublattices are the same, $m_\alpha = \rho \frac{A_u}{N_u}$, where A_u is the area of the unit cell and N_u are the number of atoms in the unit cell. Using $\mathbf{G} \cdot \mathbf{R}_n = 2n\pi$, we obtain

$$\delta u(\mathbf{r}) = \frac{1}{\sqrt{N_u}} \sum_{k\mathbf{G}} \epsilon_{k\mathbf{G}} e^{i((\mathbf{k} - \mathbf{G}) \cdot \mathbf{r} - \omega_k t)} \sqrt{\frac{\hbar N_u}{2\omega_k \rho A_u N}} a_k + h.c., \quad (\text{S24})$$

where \mathbf{r} is over the entire lattice. Writing the angular momentum

$$L^z = \frac{\hbar}{2A_u N} \int d^2 \mathbf{r} \sum_{kk'\mathbf{G}\mathbf{G}'} \left(\epsilon_{k\mathbf{G}}^\dagger M \epsilon_{k'\mathbf{G}'} \sqrt{\frac{\omega_{k'}}{\omega_k}} a_k^\dagger a_{k'} + \epsilon_{k'\mathbf{G}'}^T (-M) \epsilon_{k\mathbf{G}}^* \sqrt{\frac{\omega_k}{\omega_{k'}}} a_{k'} a_k^\dagger \right) e^{i[(\mathbf{k}' - \mathbf{G}') - (\mathbf{k} - \mathbf{G})] \cdot \mathbf{r}} e^{i(\omega_k - \omega_{k'})t}, \quad (\text{S25})$$

where we ignore the fast moving aa and $a^\dagger a^\dagger$ terms. Since \mathbf{k} runs only in the first brillouin zone and \mathbf{G} are the reciprocal lattice vectors we have $\int d^2 \mathbf{r} e^{i[\mathbf{k}' - \mathbf{G}' - (\mathbf{k} - \mathbf{G})] \cdot \mathbf{r}} = (2\pi)^2 \delta(\mathbf{k}' - \mathbf{k} - \mathbf{G}' + \mathbf{G}) \rightarrow \delta_{\mathbf{k}, \mathbf{k}'} \delta_{\mathbf{G}\mathbf{G}'} N A_u$. Therefore

$$L^z = \frac{\hbar}{2} \sum_{k\mathbf{G}} \left(\epsilon_{k\mathbf{G}}^\dagger M \epsilon_{k\mathbf{G}} a_k^\dagger a_k + \epsilon_{k\mathbf{G}}^T (-M) \epsilon_{k\mathbf{G}}^* a_k a_k^\dagger \right). \quad (\text{S26})$$

We use the properties $\epsilon_{k\mathbf{G}}^T(-M)\epsilon_{k\mathbf{G}}^* = \epsilon_{k\mathbf{G}}^\dagger M \epsilon_{k\mathbf{G}}$ and $[a_k, a_k^\dagger] = 1$ to obtain

$$L^z = \sum_k L_k^z \left(a_k^\dagger a_k + \frac{1}{2} \right). \quad (\text{S27})$$

In the main text we plot angular momentum at $k = (\mathbf{k}, \sigma)$ given by $L_k^z = \sum_{\mathbf{G}} (\epsilon_{k\mathbf{G}}^\dagger M \epsilon_{k\mathbf{G}}) \hbar$.

BERRY CURVATURE

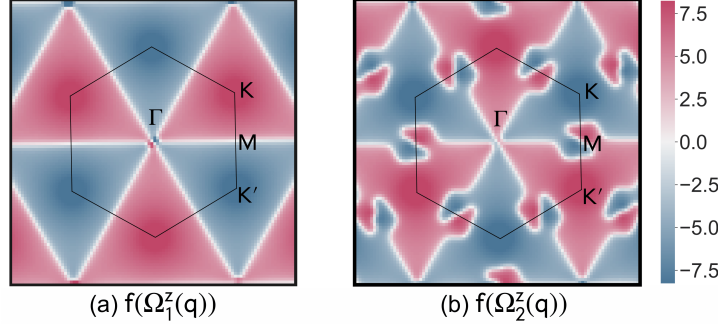


FIG. S2. The log scaled Berry curvature of (a) the lowest and (b) the second lowest phonon band in the reciprocal space for the 180° twisted bilayer MoS_2 at twist angle $\theta = 2^\circ$. The scaling function is $f(\Omega^z) = \text{sign}(\Omega^z) \ln(1 + |\Omega^z|)$

We follow the procedure in Ref.6 to calculate the phonon Berry curvature. We obtain the Hamiltonian from the Lagrangian using Legendre transformation and write it in Fourier space $H = \frac{1}{2} \sum_{\mathbf{q}} \psi_{\mathbf{q}}^\dagger H_{\mathbf{q}} \psi_{\mathbf{q}}$. We define the basis as $\psi_{\mathbf{q}} = [\delta \tilde{u}_{(\mathbf{q}-\mathbf{G})x}^-, \delta \tilde{u}_{(\mathbf{q}-\mathbf{G})y}^-, \tilde{p}_{-(\mathbf{q}-\mathbf{G})x}^-, \tilde{p}_{-(\mathbf{q}-\mathbf{G})y}^-]^T$ where each of the four operators $\delta \tilde{u}_{(\mathbf{q}-\mathbf{G})\alpha}^-$, $\tilde{p}_{(\mathbf{q}-\mathbf{G})\alpha}^-$ are N dimensional, with \mathbf{G} taking N values given by $\mathbf{G} = m_1 \mathbf{G}_1 + m_2 \mathbf{G}_2$ s.t. $m_1, m_2 \in \mathbb{Z}$. Here, we choose an appropriately large cutoff N , which is sufficient for convergence. The $4N \times 4N$ matrix $H_{\mathbf{q}}$ is given as

$$H_{\mathbf{q}} = \frac{1}{2} \begin{bmatrix} K_{\mathbf{q}} + V_{\mathbf{q}} & 0 \\ 0 & \frac{\rho}{4} I_{2N} \end{bmatrix}, \quad (\text{S28})$$

where $K_{\mathbf{q}}$ is the spring constant matrix, given as

$$K_{\mathbf{q}} = \begin{bmatrix} \text{diag}\{(\lambda + 2\mu)q_x^2 + \mu q_y^2\} & \text{diag}\{(\lambda + \mu)q_x q_y\} \\ \text{diag}\{(\lambda + \mu)q_x q_y\} & \text{diag}\{(\lambda + 2\mu)q_y^2 + \mu q_x^2\} \end{bmatrix}, \quad (\text{S29})$$

where each element is a N dimensional diagonal matrix $\text{diag}\{q\} = \text{diag}(q - G_0, \dots, q - G_{N-1})$. Similarly the interlayer interaction enters as

$$V_{\mathbf{q}} = -2V_0 \sum_j \begin{bmatrix} a_{jx}^{*2} h^j & a_{jx}^* a_{jy}^* h^j \\ a_{jx}^* a_{jy}^* h^j & a_{jy}^{*2} h^j \end{bmatrix}, \quad (\text{S30})$$

where the elements of matrix h^j are given as $(h^j)_{\mathbf{G}, \mathbf{G}'} = h_{\mathbf{G}-\mathbf{G}'}^j$. The element $h_{\mathbf{G}}^j$ is calculated as $\cos(\mathbf{G}_j \cdot \mathbf{r} + \mathbf{a}_j^* \cdot \mathbf{u}_0^- + \phi) = \sum_{\mathbf{G}} h_{\mathbf{G}}^j e^{i\mathbf{G} \cdot \mathbf{r}}$. Using the Heisenberg equation of motion $i\partial_t \psi_{\mathbf{q}} = [\psi_{\mathbf{q}}, H]$, we obtain $i\mathcal{J}\partial_t \psi_{\mathbf{q}} = H_{\mathbf{q}} \psi_{\mathbf{q}}$. The matrix $\mathcal{J} = [\psi_{\mathbf{q}}, \psi_{\mathbf{q}}^\dagger]$ is given as

$$\mathcal{J} = 2i \begin{bmatrix} 0 & I_{2N} \\ -I_{2N} & 0 \end{bmatrix}. \quad (\text{S31})$$

We solve the eigenvalue problem $\omega_{n\mathbf{q}} \mathcal{J} \psi_{n\mathbf{q}} = H_{\mathbf{q}} \psi_{n\mathbf{q}}$. The Berry curvature defined as $\Omega_n^z = \partial_{q_x} A_{ny} - \partial_{q_y} A_{nx}$, where $A_n = i \langle \psi_{n\mathbf{q}} | \mathcal{J} \partial_{\mathbf{q}} | \psi_{n\mathbf{q}} \rangle / \langle \psi_{n\mathbf{q}} | \mathcal{J} | \psi_{n\mathbf{q}} \rangle$.

We show the log-scaled berry curvature in Fig. S2 for the lowest two bands respectively in the reciprocal space. The log function is defined as $f(\Omega^z) = \text{sign}(\Omega^z) \ln(1 + |\Omega^z|)$. The symmetry properties are similar to the angular momentum discussed in the main text. The higher band is slightly dissimilar to the lower band: it has another Berry curvature hot spot as a result of anti-crossing point with a higher band at the \mathbf{M} point [see Fig. 2(b) in the main text].

EFFECTIVE MODEL

The effective model of our chiral phonons is an extension of the effective model developed for twisted bilayer graphene by Koshino and Son [1]. As we discussed in the main text, there are two contributions to the total potential energy, those associated with domain walls and those associated with domains. The domain wall potential has been discussed by Koshino and Son. It is given by [1],

$$E_{\text{DW}} = \frac{1}{2} \sum_{\mathbf{q}} \tilde{\mathbf{u}}_{-\mathbf{q}}^T D^{\text{DW}}(\mathbf{q}) \tilde{\mathbf{u}}_{\mathbf{q}}, \quad (\text{S32})$$

where

$$D_{\mu\nu}^{\text{DW}}(\mathbf{q}) = \sum_{i=1}^3 \frac{\alpha V_0 w_d}{2L_M} \left(2 \sin \frac{\mathbf{q} \cdot \mathbf{L}_i^M}{2} \right)^2 \left[\delta_{\mu\nu} - \frac{(\mathbf{L}_i^M)_\mu (\mathbf{L}_i^M)_\nu}{L_M^2} \right].$$

where $w_d \approx \frac{a}{4} \sqrt{\frac{2(\lambda+\mu)}{V_0}}$ is the width of domain walls, \mathbf{L}_i are the first star of moiré lattice vectors such that $L_M = |\mathbf{L}_i|$ [7]. It satisfies the property $D^{\text{DW}}(\mathbf{q}) = D^{\text{DW}}(-\mathbf{q})$, i.e., E_{DW} does not break C_{2z} .

In the main text, we argued that when the interlayer binding energy breaks C_{2z} symmetry, there is an additional potential energy associated with the area change of the stacking domains,

$$E_{\text{Domain}} = \frac{1}{2} \sum_{\mathbf{q}} \tilde{\mathbf{u}}_{-\mathbf{q}}^T D^{\text{Domain}}(\mathbf{q}) \tilde{\mathbf{u}}_{\mathbf{q}} = \alpha \frac{(V_{AA'} - V_{AB'})}{2} \sum_{\mathbf{q}} \tilde{\mathbf{u}}_{-\mathbf{q}}^T \begin{bmatrix} 0 & \gamma_{AA'}(\mathbf{q}) \\ -\gamma_{AA'}(\mathbf{q}) & 0 \end{bmatrix} \tilde{\mathbf{u}}_{\mathbf{q}}, \quad (\text{S33})$$

where

$$\gamma_{AA'}(\mathbf{q}) = 4i \sin\left(\frac{\mathbf{q} \cdot (\mathbf{L}_2 - \mathbf{L}_1)}{2}\right) \sin\left(\frac{\mathbf{q} \cdot \mathbf{L}_1}{2}\right) \sin\left(\frac{\mathbf{q} \cdot \mathbf{L}_2}{2}\right) \quad (\text{S34})$$

with \mathbf{L}_1 and \mathbf{L}_2 being the moiré lattice vectors. It must be noted that only bilinear terms in displacement contribute to the change in area as the linear terms average out to zero. For twisted bilayer graphene, the AA regions have the highest energy, therefore $E_{\text{Domain}} \propto V_{AB} - V_{BA}$. Since $V_{AB} = V_{BA}$, this term does not appear in Koshino and Son's model.

Combining E_{DW} and E_{Domain} together, the equation of motion is given by

$$M \ddot{\tilde{\mathbf{u}}}_{\mathbf{q}} = -[D^{\text{DW}} + D^{\text{Domain}}] \tilde{\mathbf{u}}_{\mathbf{q}}, \quad (\text{S35})$$

where $M = \rho(a/w_d)^2 w_d L_M$ is the effective mass [1]. Solving the above equation yields the phonon band dispersion of the effective model shown in Fig. 4(d) in the main text.

-
- [1] M. Koshino and Y.-W. Son, Moiré phonons in twisted bilayer graphene, Phys. Rev. B **100**, 075416 (2019).
 - [2] H. Ochoa, Moiré-pattern fluctuations and electron-phason coupling in twisted bilayer graphene, Phys. Rev. B **100**, 155426 (2019).
 - [3] S. Carr, D. Massatt, S. B. Torrisi, P. Cazeaux, M. Luskin, and E. Kaxiras, Relaxation and domain formation in incommensurate two-dimensional heterostructures, Phys. Rev. B **98**, 224102 (2018).
 - [4] L. Zhang and Q. Niu, Chiral phonons at high-symmetry points in monolayer hexagonal lattices, Phys. Rev. Lett. **115**, 115502 (2015).
 - [5] L. Zhang and Q. Niu, Angular momentum of phonons and the einstein-de haas effect, Phys. Rev. Lett. **112**, 085503 (2014).
 - [6] X. Zhang, Y. Zhang, S. Okamoto, and D. Xiao, Thermal Hall effect induced by magnon-phonon interactions, Phys. Rev. Lett. **123**, 167202 (2019).
 - [7] Koshino and Son in Ref. 1 take $2V_0$ as the binding potential energy constant compared to V_0 used in this letter. The expression for D^{DW} has a factor of half to account for the change.